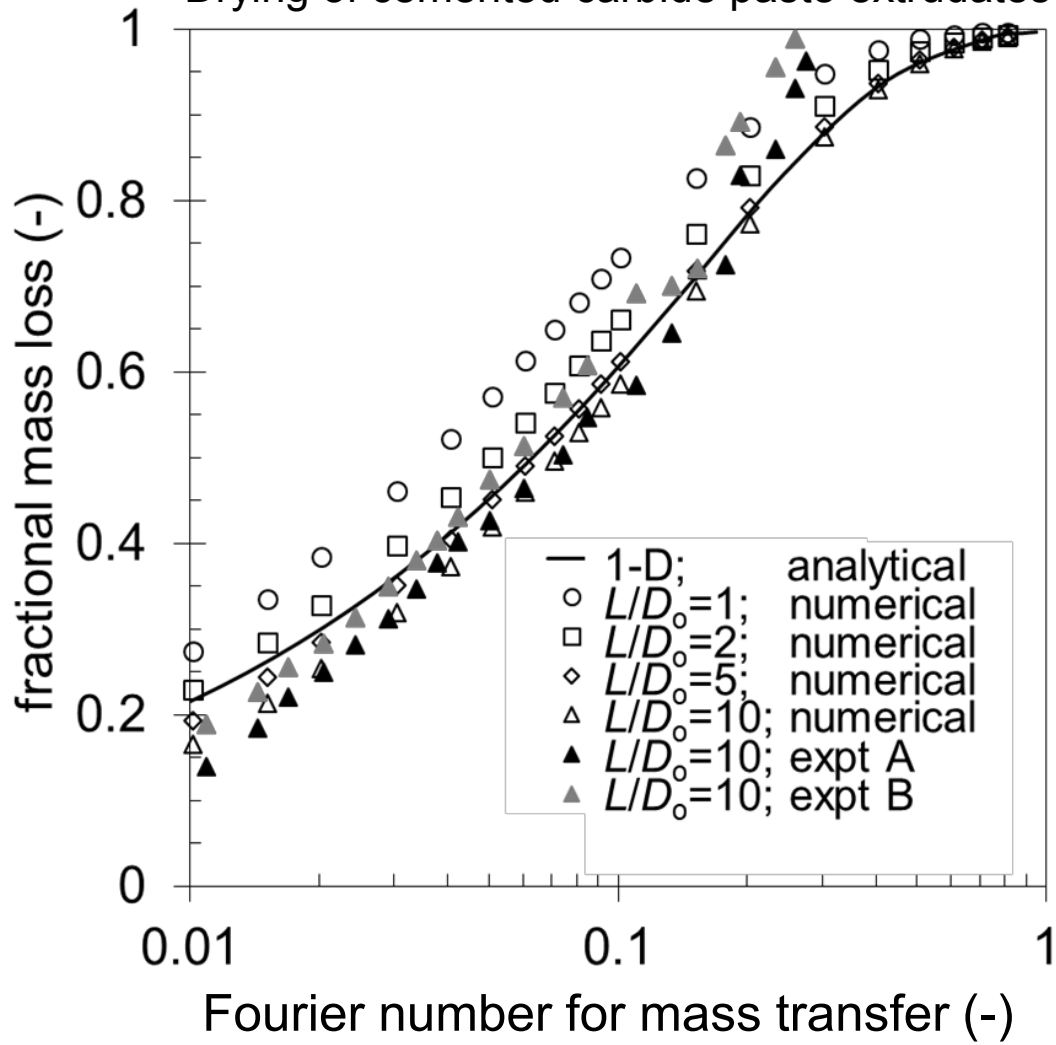


Drying of cemented carbide paste extrudates



Abstract

The drying behaviour of cemented carbide paste extrudates was investigated in an industrial drying oven at temperatures in the range 40 to 100°C. In addition to the expected evaporation of the volatile alcohol component of the paste binder, extra mass loss was recorded at the higher temperatures. This was attributed to the removal of wax present in the paste particulates. The rate of drying was investigated by removing parts periodically, weighing them and returning them to the oven. Discs, cylindrical rods and tubes with different aspect ratios were tested in order to identify a general drying model. End effects were confirmed to be important for short parts, such as rods with aspect ratio < 10 . Whilst a shrinking core model could be fitted to the disc drying data very well, it failed to describe the results for rods. A pseudo-Fickian model was found to describe all three geometries reasonably well. The effective diffusion coefficients obtained by fitting the model to the data were similar in magnitude but exhibited systematic variation with rod diameter, which were attributed to differences in strain-induced microstructure during extrusion.

Highlights

- Drying of cemented carbide paste extrudates is studied experimentally.
- Discs, cylindrical rods and tubes are tested: end effects are important.
- A shrinking core model could be fitted to the data yet failed to describe all geometries.
- A pseudo-Fickian model was found to represent all geometries adequately.

Quantifying the convective drying behaviour of cemented carbide paste extrudates

H. Ferstl^{a,b}, D.I. Wilson^b and S.L. Rough^{b*}

^a CERATIZIT Austria GmbH, 6600 Reutte, Tirol, Austria

^b Department of Chemical Engineering & Biotechnology, Philippa Fawcett Drive, West Cambridge Site, University of Cambridge, Cambridge, CB3 0AS, UK

*Corresponding author. *E-mail address:* slr1002@cam.ac.uk

1. Introduction

Near net shaping techniques, such as extrusion and powder injection moulding (PIM), are established routes for the mass production of complex ceramic and cemented carbide parts [1,2]. In these, the particulate material is combined with a liquid binder to form a paste which can be moulded readily. The liquid is often a complex fluid exhibiting non-Newtonian (*e.g.* viscoplastic) rheological behaviour. The binder is then removed in debinding processes prior to subsequent sintering to give the final product.

Since it is a temporary processing aid, the amount of binder in the paste formulation is usually minimised at the level required to provide the parts with sufficient strength to retain their shape after moulding, thereby reducing the time and energy required for debinding. The binder needs to be removed completely, avoiding contamination and component distortion in the sintering step [3]. This needs to be addressed by a careful selection of the binder composition employing constituents with different debinding characteristics. There are several debinding methods in use, which German and Bose [4] categorised as solvent and thermal processes. In solvent debinding, a liquid or vapour is used to extract the binder from the solids matrix, and is usually isothermal, whereas thermal debinding employs heat to evaporate the binder. Thermal debinding may be incorporated as the initial step of a sintering cycle, but industrial practice also includes the use of a preliminary debinding step where partial removal of a more volatile or mobile component is achieved in a cheaper ambient-pressure drying oven by thermal or wicking methods [5]. This leaves a more porous body, which eases the removal of the remaining 'backbone polymers' in the final debinding step. Popular extrusion binder formulations frequently feature water (as solvent) and cellulose ethers [6,7].

This paper presents an experimental investigation of the partial thermal debinding (hereafter referred to as drying) behaviour of discs, cylindrical rods and tubes made from a cemented carbide paste employing a proprietary organic multi-component binder system based on an alcohol and a biopolymer.

Drying involves a number of simultaneous processes determining the transport of thermal energy, mass, and the evolution of both overall dimensions and microstructure of the part [8]. For the paste extrudates under consideration here, it will be shown that the rate of internal and external heat transfer is fast compared to mass transfer. The amount of shrinkage during drying was confirmed to be small

so the process is Type I according to the classification of Liapis *et al.* [9]: the particulate structure does not change markedly during drying, although the empty pore size distribution and connectivity may change as binder is removed.

Different sample geometries are used in order to determine to what extent the results are geometry-specific, as the aim of the work is to identify a generic model for predicting the drying behaviour of more complex, industrial parts. Discs and rods both represent approximations to 1-D systems, and the tubes provide a test for the two models considered. The paper is structured thus: the experimental methods and materials are described, followed by derivations of the models. The fit of the data to the models is then discussed and conclusions drawn.

2. Experimental procedure

The drying behaviour of paste samples of various geometries in air was investigated in quasi-isothermal tests over the range 40-100°C using an industrial circulating air oven. Table 1 summarises the dimensions of the discs, rods and tubes studied.

Paste and binder

Samples were obtained as paste extrudates from a ram extruder on an industrial production line. The paste solids volume fraction was around 60% and consisted of irregularly-shaped tungsten carbide particles with a mean particle size of $\sim 1 \mu\text{m}$. Mercury porosimetry of dried parts indicated that the size of the pores present was around $0.3 \mu\text{m}$, which is consistent with the mean pore size of dried samples examined by SEM imaging. The powder also contained 10 wt% cobalt and wax as a processing aid.

The extrusion binder phase was a commercial formulation containing approximately 60 vol% of a volatile aromatic alcohol and the balance an involatile cellulose ether. The rheological behaviour of the binder and the paste has been reported previously [10].

Thermogravimetric analysis of the paste was performed in a Netzsch STA 409 CD combined TGA/DSC unit, heating a 5 g sample from 20 to 100°C over 1000 min and then holding it at 100°C for a further 1200 min. The fraction of mass lost after 2200 min was slightly larger (0.06 wt%) than the

nominal alcohol content: the difference is attributed to an additional partial evaporation of wax present in the powder and any moisture absorbed by the binder during its preparation.

For the preparation of drying samples, paste was precompacted in the extruder barrel to a maximum pressure of 3 MPa and extruded at a mean velocity of 0.06 m s^{-1} through a concentric cylindrical die. The die diameter set the (outer) diameter, D_o , of the cylindrical rods and tubes in Table 1. Discs were prepared by slicing extrudates using a water jet. Samples as thin as $\sim 3 \text{ mm}$ could be generated by this method, but the cut surfaces were somewhat gnarled. The variation in disc thickness is conveyed by the error bars in Figure 2(a).

Tubes (annular extrudates) were prepared using a similar paste. Mandrel dies were used to give tubes with an outer diameter of 12 mm and inner diameter, D_i , of 2, 4 and 8 mm. Paste preparation and extrusion protocols were similar to those used for the rod samples, but a different extruder was used for the tubes.

Drying oven

An industrial batch drying oven (David und Baader, Germany) with internal dimensions of height 1.05 m, width 0.75 m and length 1.45 m was used for the drying experiments. The oven was operated at ambient pressure. The air in the oven was recirculated by a fan operating in suction mode, located at the back of the oven, facing the door. The average air velocity in the oven of $4.7 \pm 0.2 \text{ m s}^{-1}$ was measured at 40°C using a thermal anemometer (testo 425, Testo, Germany). This gave a Reynolds number of 250,000 for the oven, based on a hydraulic diameter of 0.875 m, indicating that the air flow in the oven was in the turbulent regime. Turbulence and eddies were intensified by internal fittings such as the loading rack and plates supporting the dry parts. Heating of the air was provided by electrical devices located on the cavity sides. A fraction of the air was exhausted *via* an outlet valve and replaced by ambient air: its temperature and humidity were not controlled. The air purge prevented the atmosphere becoming saturated with evaporated binder components and hence a number of parts could be dried to completion.

Drying experiments

Tests were performed in triplicate. Discs were dried while resting on bent gauze mats located within petri dishes ensuring full exposure to the air flow in the oven, whereas rod and tube samples were placed on baking paper in order to ease the transfer of samples for weighing. A flat graphite support base was used for the cylindrical geometries to minimise unsymmetrical air flow around the diameter. The cylindrical parts were positioned in the oven so that the drying air flow was parallel to their longitudinal axis. An external balance (Kern PLJ 600-3NM, ± 0.005 g) was used to determine the sample mass. All the samples were taken out of the oven at a given time and weighed. The weighing of sets of samples employed in a single test run took up to 10 min and was done at ambient temperature, after which the samples were returned to the oven. The weighing times were not included in the total drying time. The frequency of weighing was a compromise between suitable resolution of mass loss and the time required by the samples to return to the test temperature. Quasi-isothermal drying conditions were also affected by the opening of the oven door to remove/replace samples for external weighing, which caused a decrease in the oven air temperature. This was then followed by an over-compensation by the oven temperature controller once the door had been shut. These deviations from the isothermal drying conditions were not considered in the data analysis: the time periods were short compared to the overall drying time of the samples. This assumption was checked by determining the mass loss of control samples which were only removed for weighing at the end of a drying test: this was found to be similar to those of samples subjected to regular weighing *ex situ*.

Drying of paste materials can be accompanied by considerable shrinkage depending on their respective liquid/solid ratio (*e.g.* [11]). As the solid content of the extrusion pastes used in this study approached the maximum solids loading, where the particles are separated from each other only by a thin layer of binder material, shrinkage during the evaporation of the binder during drying was expected to be small. This was confirmed by measurements on the parts before and after drying, which showed that radial and axial shrinkage was less than 0.1%.

The fraction of mass lost at the end of the drying experiments, denoted Δm_{end} , did not match the alcohol content, m_{alc} , observed in the TGA tests. Figure 1 shows the evolution of mass loss for $D_o = 30.2$ mm discs ($D_o/H = 20$, where H is the half-thickness of the disc samples) at different temperatures, plotted in terms of the observed mass loss, Δm , divided by the alcohol content. The rate

of mass loss increases with temperature, and Δm_{end} exceeds the alcohol content above 50°C. Similar behaviour was observed for rods and tubes. The ratio of $\Delta m_{\text{end}}/m_{\text{alc}}$ depended on the temperature and aspect ratio of the part and is summarised for each geometry in Figure 2. The excess in mass loss is attributed primarily to the wax content of the powder, although absorbed water could also contribute. Inspection of the oven's outlet vent after the tests revealed some waxy material there, indicating that the alcohol in the binder promoted dissolution of the wax and its subsequent partial evaporation. Owing to the indeterminate nature of the evaporated species, all subsequent model fitting used an estimate of Δm_{inf} based on measured mass loss at long drying times, Δm_{end} , rather than the notional alcohol content. This correction means that the values of the diffusion coefficients calculated from the data will incorporate a systematic change in vapour composition due to temperature.

Heat transfer aspects

Some preparatory testing was conducted to establish the relative rates of heat and mass transfer within the parts and in the drying oven. The thermal conductivities of the paste and dried parts were measured using a commercial Hot Disk™ device and the guarded hot plate apparatus described by Lister *et al.* [12]. These gave similar values of thermal conductivity, at $1.57 \pm 0.06 \text{ W m}^{-1}\text{K}^{-1}$ for the fresh paste and $1.49 \pm 0.04 \text{ W m}^{-1}\text{K}^{-1}$ for the dried part, indicating that heat conduction in the parts was dominated by particle contacts. The corresponding values of thermal diffusivity were 0.69 ± 0.06 and $0.63 \pm 0.09 \times 10^{-6} \text{ m}^2 \text{ s}^{-1}$. Fitting the drying data to the pseudo-Fickian drying model, reported later, gave effective mass diffusivity values of order $10^{-10} \text{ m}^2 \text{ s}^{-1}$, indicating that internal mass transfer is much slower than internal heat transfer.

The rate of external convective heat transfer to internal conduction was quantified by performing transient heat transfer experiments with copper discs and rods of similar dimensions to the extrudates. A thermocouple was located at the midpoint of the disc or rod, and the time to respond to a step change in temperature (i.e. by placing the part in the oven) was recorded. The thermal conductivity of the copper is large, so the part can be treated as effectively isothermal and heating is controlled externally by the convective film heat transfer coefficient from the air to the sample, h . Values of h were obtained by fitting temperature-time data to a lumped parameter model: for a rod,

$$\ln \left(\frac{T_{\text{Cu}}(t) - T_{\text{air}}}{T_{\text{Cu}}(0) - T_{\text{air}}} \right) = - \frac{hA}{mC_{p,\text{Cu}}} t \quad (1)$$

where $T_{\text{Cu}}(t)$ is the temperature of the copper sample at a specific time t , T_{air} the temperature of the air in the oven and $T_{\text{Cu}}(0)$ the initial temperature of the copper rods (here room temperature). A is the sample area available for heat transfer, m the sample mass and $C_{p,\text{Cu}}$ is the specific heat capacity of copper. This gave h values ranging from $33 \pm 2 \text{ W m}^{-2}\text{K}^{-1}$ for rods with $D_o = 12 \text{ mm}$, $L = 24 \text{ mm}$ heated to a final temperature of 100°C , to $78 \pm 4 \text{ W m}^{-2}\text{K}^{-1}$ for rods with $D_o = 20.5 \text{ mm}$, $L = 80 \text{ mm}$ heated to 40°C .

A Biot number for heat transfer for the rods can be defined as $Bi_H = hD_o/4k$, where k is the thermal conductivity. For heat transfer to be internally controlled, Bi_H should be greater than 1, whereas external control is expected for $Bi_H < 0.1$ [13]. The values for the copper samples lay in the range 0.0002-0.001, therefore confirming external heat transfer control. The Biot numbers for heat transfer for the extruded and (partly-) dried cemented carbide parts, with noticeably smaller thermal diffusivity, lay in the range 0.2-1.6, indicating that internal conduction was important for heat transfer. Given the difference in thermal and mass diffusivities, however, this contribution was deemed small.

3. Modelling

The drying experiments record the change in the total mass of a part over time, which can be fitted to expressions based on lumped models (*e.g.* [14]) or more detailed numerical simulations (*e.g.* [15]). The literature contains many empirical expressions to describe the extent of drying, but applying these results to different geometries is not straightforward. Ideally, the spatial distribution of the species of interest would be measured and compared with the predictions of a detailed model in order to verify its accuracy. This is a challenge for cemented carbide extrudates considered here, as the high density of the solids precludes the use of tomographic techniques such as magnetic resonance imaging and X-ray microtomography over the length scales of interest. The approach taken was thus to compare the experimental data with two simple analytical models representative of those used for other materials to establish which gave a more consistent description of the data. Since the oven was purged with fresh air, modelling of the external mass transfer resistance as a function of the level of saturation of the drying air could be omitted.

Shrinking core

This model is frequently used to describe drying in ceramics [16] and was fitted to the disc and rod drying data. Drying is assumed to exhibit a sharp front, delineating the debinded region from that containing binder. The front moves inward from the outer surface with drying time t , as depicted in Figure 3 for an infinitely long cylinder of radius R . The process is isothermal and enthalpy changes are assumed to be small, so the rate of mass loss is controlled by Fickian diffusion of evaporated binder across the annulus of 'dried' material. Knudsen diffusion is not expected to be significant as the pore sizes are expected to be of order 250 nm and the mean free path of the vapour is approximately 100 nm. The steady-state diffusion equation is used to describe the concentration, C , of the evaporated species in the annulus:

$$D_{sc} \frac{d}{dr} \left(r \frac{dC}{dr} \right) = 0 \quad (r^* \leq r \leq R) \quad (2)$$

where r^* is the radial location of the drying front and D_{sc} is the effective diffusion coefficient of the evaporated species through the dried region. D_{sc} includes contributions from the diffusion coefficient of the evaporating species through the vapour in the pores, the porosity and the connectivity of the channels.

The initial condition is:

$$C = C_0, \quad 0 \leq r \leq R, \quad t < 0 \quad (3)$$

The boundary conditions are

$$C = 0, \quad r = R, \quad t \geq 0 \quad (4)$$

$$C = C^*, \quad r = r^*, \text{ for } r^* < R, \quad t \geq 0 \quad (5)$$

C_0 is the initial concentration of evaporating species within the part (assumed to be constant) and C^* is the equilibrium concentration at the drying front. Instantaneous steady state is assumed, so that the rate of evaporation at the drying front is equal to the rate of mass loss, giving:

$$1 - \left(\frac{r^*}{R} \right)^2 \left[1 - \ln \left(\frac{r^*}{R} \right)^2 \right] = k_{sc} t \quad (6)$$

where the rate parameter, k_{sc} , is given by:

$$k_{sc} = \frac{4D_{sc} C^*}{R^2 C_0} \quad (7)$$

Assuming a uniform distribution of evaporating species throughout the part and initial mass of volatiles m_{vol} , Equation (6) can then be written in terms of the overall mass loss, Δm , more conveniently in terms of the parameter W , defined thus:

$$W \equiv \frac{\Delta m}{m_{\text{vol}}} + \left(1 - \frac{\Delta m}{m_{\text{vol}}}\right) \ln \left(1 - \frac{\Delta m}{m_{\text{vol}}}\right) = k_{\text{sc}} t \quad (8)$$

The equivalent expression for an infinitely wide slab of thickness $2H$ is

$$\frac{\Delta m}{m_{\text{vol}}} = \left(\frac{2D_{\text{sc}} C^*}{H^2 C_0}\right)^{1/2} t^{1/2} = (k_{\text{sc}} t)^{1/2} \quad (9)$$

Equations (8) and (9) feature different temporal relationships for the cylindrical and slab geometries, so it is important to consider the likely contribution from the ends of a rod and the sides of a disc to the overall behaviour. A simple way of quantifying this is to calculate the area of the faces being modelled to the total area of the part, *e.g.* the ratio of the curved surface area of a rod to its total external area (curved + two end faces). Figure 4 presents this ratio with the values for the disc and rod geometries used in this work. For a given aspect ratio, the contribution from the ends is noticeably smaller for the rods than for the discs. Supplementary Figure S1 shows that faster drying was observed with the smallest disc ($D_0 = 12$ mm), while Figure S2 shows that shorter rods dried faster. End effects therefore needed to be considered, particularly if experimental data are to be compared with 1-D analytical results.

Pseudo-Fickian diffusion

The experimental data were also compared with the solutions to the transient diffusion equation, which is commonly used to describe drying phenomena and which can be readily applied to more complex geometries:

$$D_{\text{eff}} \frac{\partial^2 C}{\partial z^2} = \frac{\partial C}{\partial t} \quad (10)$$

where D_{eff} is the effective diffusivity. Solutions to Equation (10) for 1-D slabs, rods and annuli reported by Crank [17] were compared with the experimental data: the initial concentration of volatile component is again assumed to be uniform, at C_0 , and D_{eff} was assumed to be isotropic, uniform and constant at a given temperature. The values for D_{eff} should be independent of the sample geometry provided that end effects are small or are accounted for in numerical solutions.

Interpretation of the terms C and D_{eff} requires care. Whereas in the shrinking core model C and D_{eff} can be directly related to parameters of the vapour phase, they are mathematical constructs in this case. The volume of the vapour and binder phase in the pores at a particular location changes with time, but as an ensemble quantity C contains contributions from both phases: it will be biased towards

liquid present owing to its higher density. Likewise D_{eff} is likely to be biased towards vapour phase transport. Detailed pore-scale models, including local equilibrium such as those reported by Prat [18], are required to give physically meaningful parameters. It should also be noted that D_{eff} is in general a function of temperature, the content of the volatile species and the microstructure, *i.e.* porosity [13]. However, in the absence of the discrete material composition and structure at a given drying state, the assumption of a constant D_{eff} value in isothermal drying tests remains a valid approach.

Disc drying

End effects are neglected so that debinding is modelled as diffusion in a slab of thickness $2H$. The system is symmetrical about the central plane, set at $z = 0$, with external surfaces at $z = \pm H$. The local concentration of volatile component C obeys the following initial and boundary conditions:

$$C = C_0, \quad -H < z < H, \quad t < 0 \quad (11)$$

$$C = 0, \quad z = \pm H, \quad t \geq 0 \quad (12)$$

$$\frac{\partial C}{\partial z} = 0, \quad z = 0, \quad t \geq 0 \quad (13)$$

The total amount of volatile having left the slab is given by [17]:

$$\frac{\Delta m}{\Delta m_{\text{inf}}} = 1 - \sum_{n=0}^{\infty} \frac{8}{(2n+1)^2 \pi^2} \exp\left\{-\frac{\pi^2}{4} (2n+1)^2 \frac{D_{\text{eff}} t}{H^2}\right\} \quad (14)$$

where Δm_{inf} is the mass loss after infinite time.

The argument of the exponential terms contains the Fourier number for mass transfer, Fo_M , *viz.* $\frac{D_{\text{eff}} t}{H^2}$. At small times, where $\Delta m / \Delta m_{\text{inf}} < 0.5$, the mass loss can be approximated with little error by [19]:

$$\frac{\Delta m}{\Delta m_{\text{inf}}} = 2 \left(\frac{D_{\text{eff}} t}{\pi H^2} \right)^{1/2} \quad (15)$$

D_{eff} can then be estimated graphically by inspection of the initial gradient of a plot of dimensionless mass loss against $t^{1/2}$. Initial estimates of D_{eff} were obtained using this approach and the full expression evaluated to show the agreement with the model.

Other geometries

The corresponding result for a long cylindrical rod is

$$\frac{\Delta m}{\Delta m_{\text{inf}}} = 1 - \sum_{n=1}^{\infty} \frac{4}{R^2 \alpha_n^2} \exp(-D_{\text{eff}} \alpha_n^2 t) \quad (16)$$

where the α_n terms are the roots of the Bessel function of the first kind of order zero, J_0 , *i.e.*

$$J_0(R\alpha_n) = 0 \quad (17)$$

and for a tube, *i.e.* a long annulus with inner and outer radii R_i and R_o , respectively

$$\frac{\Delta m}{\Delta m_{\text{inf}}} = 1 - \frac{4}{(R_o^2 - R_i^2)} \sum_{n=1}^{\infty} \frac{J_0(R_i\alpha_n) - J_0(R_o\alpha_n)}{\alpha_n^2 \{J_0(R_i\alpha_n) + J_0(R_o\alpha_n)\}} \exp(-D_{\text{eff}}\alpha_n^2 t) \quad (18)$$

where the parameters $R\alpha_n$ are the positive roots of:

$$J_0(R_i\alpha_n)Y_0(R_o\alpha_n) - Y_0(R_i\alpha_n)J_0(R_o\alpha_n) = 0 \quad (19)$$

and Y_0 is the Bessel function of the second kind of order zero.

End effects

The effect of sample geometry on overall drying behaviour was considered for an ideal 2-D axisymmetric case using the COMSOL[®] Multiphysics simulation package. A series of simulations were performed for cylindrical rods of finite length with aspect ratios covering the range used in the experiments. The spatial distribution of concentration at various times integrated to give a volume-averaged concentration for comparison with Eqn. (16). D_{eff} values representative of those extracted from experiments at 60°C were used in the calculations. Times are presented in terms of the Fourier number for mass transfer, FO_M , *viz.*:

$$FO_M = \frac{D_{\text{eff}}t}{R^2} \quad (20)$$

The geometry was defined for a quarter rod and symmetry conditions imposed at the radial boundaries. Meshing was performed by the software's built-in mesh generator and yielded, depending on the aspect ratio, up to ~270,000 triangular mesh elements. Time-dependent solutions were generated by the PARADISO solver, taking less than one minute to converge on a desktop PC to an absolute error in C of less than 10^{-5} where $C_0 = 1$ arbitrary unit.

Concentration plots showed that the influence of an end face extended approximately one radius into the rod. The effect on total mass loss is presented in Figure 5, which shows that short rods lose noticeably more material in the early stages, but approach complete drying at similar FO_M (~0.8). Any estimate of D_{eff} based on the initial drying behaviour will then be subject to a systematic error. Also plotted are the 1-D result (Equation (16)) and two sets of experimental data obtained with long rods ($L/D_o = 10$) at 60°C. Figure 4 indicates that such rods feature a cylindrical surface area fraction of

95%. The experimental data show reasonable agreement with the analytical and computed results for $0.2 < \Delta m/\Delta m_{\text{inf}} < 0.8$, suggesting that this part of the profile should be used for estimating D_{eff} . The plot confirms that generating (and handling) long uniform rods is highly desirable for modelling. However, it can be challenging to prepare and handle such parts in practice.

4. Results and Discussion

Shrinking core modelling

Figure 6 shows examples of fitting Equation (8) to experimental data obtained with long rods (where end effects are expected to be small) at drying temperatures of 40°C and 100°C. The agreement is reasonable at both temperatures: similarly favourable results were obtained in other tests. The gradient yields an estimate of the shrinking core rate parameter, k_{SC} , which should be proportional to R^2 according to Equation (7). The plots in Figure 6(c) and (d) show a linear dependency on R^2 , but with a non-zero intercept, indicating that the model does not capture the effect of length scale correctly. Whilst interpolation could be used to predict drying performance for rods of intermediate size, its usefulness for more complex geometries is limited.

Further reason to avoid using the shrinking core model is that the data sets from disc drying did not follow the trend predicted by Equation (9) (see Supplementary Figure S3). This result confirms the need to conduct tests with different geometries to establish the general applicability of a model. Comparisons of tube drying data with the shrinking core model were consequently not performed.

A final reason to avoid using the shrinking core model was that the temperature dependency observed in k_{SC} values was weaker than that expected from Equation (7). The diffusion coefficient should increase with absolute temperature as $T^{1.75}$ for Fickian diffusion and $T^{0.5}$ for Knudsen diffusion. Whilst C_0 is expected to be independent of temperature, the equilibrium concentration C^* is expected to increase strongly with temperature following the Clausius-Clapeyron relationship. Using data from literature, C^* for the alcohol is predicted to increase around 60-fold over the temperature range studied. Therefore, assuming Fickian diffusion, k_{SC} is expected to increase by a factor of 80 for a given value of R . However, analysis of the experimental data using the shrinking core model predicts only a ten-fold increase in k_{SC} . Pseudo-Arrhenius plots of $\ln k_{\text{SC}}$ against $1/T$ (see Supplementary Figure S4)

gave linear trends with activation energies ranging from 37.7 ± 0.4 to 40.4 ± 0.2 kJ mol⁻¹, which are typical of processes characterised by mass transfer control [20], *i.e.* diffusion alone, with the volatility of the binder having little influence.

The assumptions of a sharp drying front and uniform diffusion coefficient are probably inaccurate as the particles used in the cemented carbide parts are non-spherical and are likely to have been orientated by extrusion, giving a range of pore sizes and potentially anisotropic properties. The largest pores are expected to lose binder first, so the distribution of binder-free pores is expected to change with time. Including detailed considerations such as locally time-dependent porosity in a quantitative model was not attempted, although it has been applied for other systems (*e.g.* in grain models of chemical reaction of porous solids [21], and soil drying [22]).

Pseudo-Fickian diffusion in discs and rods

The Fickian expressions (Eqs 14 and 16) could be fitted to the data sets for both discs and rods with reasonable agreement, unlike the shrinking core model. Figure 7 shows examples of data fitting for the two geometries, and includes cases which gave good agreement and others with noticeable deviation. In most cases the models fitted well up to $\Delta m/m_{\text{inf}} \approx 0.8$, the region beyond which is interpreted as where differences in porosity and microstructure would be most noticeable. The values of D_{eff} are of similar magnitude, of order 10^{-10} m²s⁻¹, and are similar to the D_{eff} values reported for the drying of water-based alumina suspensions for tape casting by Briscoe *et al.* [23] and Puyate and Lawrence [24]. Pourcel *et al.* [25] reported a D_{eff} value of 5×10^{-9} m² s⁻¹ for the drying of an alumina gel, which was weakly dependent on both moisture content and temperature. Marinos-Kouris and Maroulis [13] listed diffusivities for a range of materials, with D_{eff} values for concrete ranging from 5.0×10^{-10} to 1.2×10^{-8} m² s⁻¹.

The values of D_{eff} extracted from the disc and rod data sets are summarised in Tables 2 and 3, respectively. D_{eff} increases with temperature for both disc and rod geometries, the magnitude being dependent on the size and shape of the part. Figure 8(a) shows the effect of temperature on D_{eff} for discs, plotted in the form of the pseudo-Arrhenius relationship [13]:

$$D_{\text{eff}} = D_{\text{ref}} \exp\left(-\frac{E_{\text{D}}}{R_{\text{g}}T}\right) \quad (19)$$

where R_g is the gas constant, D_{ref} a prefactor and E_D an activation energy for a diffusive process. At a given temperature, the D_{eff} values for the different disc diameters follow the order expected owing to the contribution from edge effects, increasing as disc diameter and hence D_o/H decrease. The values of E_D lie in the range 27-32 kJ mol⁻¹, which are comparable to the 37 kJ mol⁻¹ reported by Briscoe *et al.* [23].

For the rods, D_{eff} also increases with temperature for samples of similar diameter and aspect ratio. The activation energies obtained from the plots in Figure 8(b) and eight other sets (data not reported) lay around 25 kJ mol⁻¹, which is slightly lower than those obtained from the disc tests.

Figure 8(b) also shows a systematic dependency on the rod diameter D_o beyond that predicted by the model, also seen in the k_{sc} values obtained for the shrinking core model (Figure S4).

Inspection of the D_{eff} values for rods in Table 3 shows a decrease with increasing L/D_o at a given temperature and diameter, which is attributed to end effects becoming less of an issue. The values of D_{eff} also increase with increasing D_o for a given L/D_o for all temperatures (see Figure 8(b)). D_{eff} for the 12 and 30.2 mm diameter rods differ by up to a factor of three. The effect of D_o on D_{eff} is presented in Figure 9, where D_{eff} values for rods are plotted against the value obtained for the 30.2 mm diameter disc at the same temperature (as this is expected to give the best approximation to a 1-D slab). The values for the $D_o = 12.0$ mm rods are smaller than those for the disc; the 20.5 mm values at $L/D_o = 10$ approach the disc value, but are larger for $L/D_o = 2$ (due to end effects); the 30.2 mm values at $L/D_o = 2$ are larger still (again due to end effects). If it had been possible to study long rods with 30.2 mm diameter, the D_{eff} values would be expected to match those of the discs. In all cases, the difference increases with temperature.

The following explanations for this behaviour were considered:

- (i) Artefacts in disc preparation. The discs were prepared by water jet cutting, which introduces an unquantifiable degree of disruption to the surface microstructure and thus its transport properties. Cutting will have relatively modest effect on rods. Cutting effects apply to all disc sizes and could explain differences between discs and rods, but not the influence of rod diameter.

- (ii) Differences in flow-induced microstructure. There are two sources of flow-induced microstructure: firstly, flow of the paste along the die land is subject to significant wall slip and material next to the wall will be subject to wall effects. This region is expected to be thin and would not be expected to contribute markedly to the axial diffusivity, which is the dominant contribution to the disc D_{eff} values.

The second is the strain experienced by the paste as it enters the die land from the barrel. The extrudates were generated using the same barrel and the engineering strain at the die entry can be approximated in the first instance by $\ln(D_{\text{barrel}}/D_0)$ [26]: the additional strain experienced by the paste in making the 20.5 mm and 12.0 mm rods was 0.39 and 0.92, respectively. The additional strain (and associated orientation) is postulated to impart more alignment of particles within the extrudate (*e.g.* [27,28]), thus creating an anisotropic diffusivity. Direct measurement of the microstructure is challenging as the high density of the tungsten carbide is not conducive to imaging, and porosimetry does not provide information on alignment.

Further work is required to elucidate the effect of rod diameter, including comparing the data with more sophisticated models such as those described by Mujumdar and Tsotsas [29].

Tubes

Drying profiles obtained for tubes with $D_0 = 12.0$ mm and $L/D_0 = 10$ at 50°C and 90°C are presented in Figure 10 alongside data sets obtained for a 12.0 mm diameter rod under the same conditions. The drying time increases as the initial mass of binder to be removed increases. The profiles show very good fits to the model (Equation (18)) and the values of D_{eff} obtained are listed in Table 4. The agreement between each annulus width and the solid rod is considered to be good, given the uncertainties in the material and use of a different extruder for rods and tubes. Internal radial diffusion is expected to dominate mass transfer in the drying of these tubes, so the agreement with a rod of similar D_0 (and thus strain history) is expected.

5. Conclusions

The drying of cemented carbide paste extrudates was investigated over a wide range of temperatures and using three different sample geometries to identify the most appropriate modelling approach to

describe the removal of the alcohol component of the paste binder from the parts. The mass loss data indicated that some of the wax material added as an extrusion aid was being removed in addition to the alcohol, with the amount increasing with drying temperature. The mass transfer parameters calculated in the modelling work therefore contain some variation associated with changes in composition, which would need to be considered if the paste composition is altered.

Drying is frequently modelled by the shrinking core model. This model fitted the drying of rods reasonably well but gave parameters inconsistent with the model assumptions, and it did not fit the data obtained with discs.

Fickian-diffusion based approaches were found to give acceptable descriptions of the experimental data. End effect contributions were found to be significant, and the likely impact was quantified using 2-D simulations assuming constant and isotropic diffusion coefficients. The diffusion coefficients obtained from fitting to Crank's analytical results for discs, rods and tubes all gave diffusivities of order $10^{-10} \text{ m}^2 \text{ s}^{-1}$, which increased with temperature, in line with previous studies in the literature. The values obtained for rods and discs under identical conditions showed systematic differences with extrudate diameter, which are attributed to flow-induced structuring during extrusion.

Acknowledgements

Project funding from Ceratizit Austria GmbH is gratefully acknowledged, as are TGA measurements by Dr P. Schoderböck and the assistance of A. and C. Zobl in the drying experiments.

Nomenclature

List of symbols

A	area	m^2
Bi_H	Biot number for heat transfer	-
C, C_o, C^*	concentration, initial value, equilibrium value	arbitrary units
C_p	specific heat capacity	$\text{J kg}^{-1} \text{K}^{-1}$
D_{barrel}	extruder barrel diameter	m
D_{eff}	effective diffusion coefficient	$\text{m}^2 \text{s}^{-1}$

D_{sc}	diffusion coefficient, shrinking core model	$m^2 s^{-1}$
D_i	(inner) diameter of tube samples	m
D_o	(outer) diameter of disc, rod and tube samples	m
D_{ref}	prefactor, Equation (19)	$m^2 s^{-1}$
E_D	activation energy for diffusion	$J mol^{-1}$
E_{ksc}	activation energy for shrinking core model rate parameter	$J mol^{-1}$
Fo_M	Fourier number for mass transfer	-
h	heat transfer coefficient	$W m^{-2} K^{-1}$
H	half-thickness of disc	m
J_0, J_1	Bessel function of first kind	-
k	thermal conductivity	$W m^{-1} K^{-1}$
k_{sc}	rate parameter, shrinking core model	s^{-1}
L	rod or tube length	m
m	mass	kg
n	index in summations	-
r	radial co-ordinate	m
r^*	radial location of shrinking front	m
R, R_i, R_o	radius, inner radius, outer radius	m
R_g	gas constant	$J mol^{-1} K^{-1}$
t	time	s
T	temperature	K
W	mass ratio, Equation (8)	-
Y_0, Y_1	Bessel function of second kind	-
z	linear co-ordinate	m
α	root of Bessel function, Equation (17)	m^{-1}

Subscripts

air	air
alc	alcohol
Cu	copper

end at end of drying
inf at long drying times
vol of volatiles

References

- [1] J. Powell, S. Blackburn, Co-extrusion of multilayered ceramic micro-tubes for use as solid oxide fuel cells, *J. Eur. Ceram. Soc.* 30 (14) (2010) 2859-2870.
- [2] M.T. Martyn, P.J. James, The processing of hardmetal components by powder injection moulding, *Int. J. Refrac. Metals and Hard Mat.* 12 (2) (1993-1994) 61-69.
- [3] R.M. German, Theory of thermal debinding, *Int. J. Powder Metallurgy* 23 (4) (1987) 237-245.
- [4] R.M. German, A. Bose (Eds.), *Injection Molding of Metals and Ceramics*, MPIF, Princeton, 1997.
- [5] I.M. Somasundram, A. Cendrowicz, M.L. Johns, D.I. Wilson, A phenomenological study and modelling of wick debinding, *Chem. Eng. Sci.* 63 (14) (2008) 3802-3809.
- [6] R.J. Huzzard, S. Blackburn, A water-based system for ceramic injection moulding, *J. Eur. Ceram. Soc.* 17 (1997) 211-216.
- [7] R. Bayer, M. Knarr, Thermal precipitation or gelling behaviour of dissolved methylcellulose derivatives – Behaviour in water and influence on the extrusion of ceramic pastes. Part 1: Fundamentals of MC-derivatives, *J. Eur. Ceram. Soc.* 32 (2012) 1007-1018.
- [8] T.A. Ring, *Fundamentals of Ceramic Powder Processing and Synthesis*, Academic Press, London, 1996.
- [9] A.I. Liapis, J.C. Wang, R. Bruttini, Practical benefits for the separation process of drying that can be realized from novel multiscale modelling procedures that utilize the scientific information and results obtained from molecular dynamics modelling and simulation studied, *Dry. Tech.* 34(15) (2016) 1753-1757.
- [10] H. Ferstl, R. Barbist, S.L. Rough, D.I. Wilson, Influence of visco-elastic binder properties on ram extrusion of a hardmetal paste, *J. Mat. Sci.* 47 (2012) 6835-6848.
- [11] R. Misra, A.J. Barker, J. East, Controlled drying to enhance properties of technical ceramics, *Chem. Eng. J.* 86 (2002) 111-116.
- [12] V.Y. Lister, J.F. Davidson, S.J. Sutcliffe, D.I. Wilson, Management of acute particulate fouling in a titanium dioxide reactor system, *Heat Transf. Eng.* 38 (7-8) (2017) 796-804.
- [13] D. Marinos-Kouris, Z.B. Maroulis, Transport properties in the drying of solids, in: A. Mujumdar, (Ed.), *Handbook of Industrial Drying*, 3rd ed., Taylor & Francis Group, Boca Raton, 2006, pp. 81-119.
- [14] J.J.d.S Nascimento, A.G.B Lima, E.W.F. Santana, F.A. Belo, G.d.A. Neves, L.N. Santana,

- V.R. Batista, Experimental drying of ceramic bricks including shrinkage, Proc. of COBEM 2005, Ouro Preto, MG, Brazil.
- [15] T. Metzger, M. Kwapinska, M Peglow, G. Saage, E. Tsotsas, Modern modelling methods in drying, Trans. in Porous Media 66 (2007) 103-120.
- [16] Z. Shi, Z.X. Guo, J.H. Song, A diffusion-controlled kinetic model for binder burnout in a powder compact, Acta Mat. 50 (2002) 1937-1950.
- [17] J. Crank, The Mathematics of Diffusion, 2nd ed., Clarendon Press, Oxford, 1975.
- [18] M. Prat, Pore network models of drying, contact angle, and film flows, Chem. Eng. Tech. 34 (7) (2011) 1029-1038.
- [19] E.C. Suloff, Sorption behaviour of an aliphatic series of aldehydes in the presence of poly(ethylene terephthalate) blends containing aldehyde scavenging agents. PhD thesis, Virginia Polytechnic Institute and State University, 2002.
- [20] O. Levenspiel, Chemical Reaction Engineering, 3rd ed., Wiley, New York, 1999.
- [21] C. Georgakis, C.W. Chang, J. Szekeley, A changing grain size model for gas-solid reaction, Chem. Eng. Sci. 34(8) (1979) 1072-1075.
- [22] L.B. Hu, H. Péron, T. Hueckel, T. L. Laloui, Mechanisms and critical properties in drying shrinkage of soils: experimental and numerical parametric studies, Canadian Geotech. J. 50(5) (2013), 536-549.
- [23] B.J. Briscoe, G. Lo Biundo, N. Özkan, Drying kinetics of water-based ceramic suspensions for tape casting, Ceram. Int. 24 (1998) 347-357.
- [24] Y.T. Puyate, C.J. Lawrence, Sherwood's models for the falling-rate period: A missing link at moderate drying intensity, Chem. Eng. Sci. 61 (21) (2006) 7177-7183.
- [25] F. Pourcel, W. Jomaa, J.R. Puiggali, L. Rouleau, Criterion for crack initiation during drying: alumina porous ceramic strength improvement, Powder Tech. 172 (2007) 120-127.
- [26] M.P. Bryan, S.L. Rough, D.I. Wilson, Flow visualisation and modelling of solid soap extrusion, Chem. Eng. Sci. 173 (2017) 110-120.
- [27] T. Zhang, S. Blackburn, J. Bridgwater, The orientation of binders and particles during ceramic injection moulding, J. Eur. Ceram. Soc. 17(1) (1997) 101-108.
- [28] T. Isobe, Y. Kameshima, A. Nakajima, K. Okada, Preparation and properties of porous ceramics with uni-directionally orientated pores by extrusion method using a plastic substance as a pore former, J. Eur. Ceram. Soc. 27(1) (2007) 61-66.

- [29] A. Mujumdar, E. Tsotsas (Eds.), *Modern Drying Technology, Volume 1: Computational tools at different scales*, Wiley, Weinheim, 2007.

Table captions

Table 1 Sample geometries, dimensions and test temperatures for the isothermal drying tests. Ticks indicate the tests performed. For meaning of symbols, see nomenclature.

Table 2 Averaged D_{eff} values (in $10^{-10} \text{ m}^2 \text{ s}^{-1}$) from triplicate tests for drying of disc samples.

Table 3 Averaged D_{eff} values (in $10^{-10} \text{ m}^2 \text{ s}^{-1}$) from triplicate tests for rod samples. (-) indicates that no test was performed.

Table 4 Averaged D_{eff} values (in $10^{-10} \text{ m}^2 \text{ s}^{-1}$) from triplicate tests for extruded tube and rod samples with $D_o = 12.0 \text{ mm}$ and $L/D_o = 10$.

List of Figure captions

Figure 1 Effect of temperature on mass loss for $D_o = 30.2$ mm, $H = 1.5$ mm discs. Horizontal dashed line indicates $\Delta m = m_{alc}$.

Figure 2 Effect of temperature on averaged final mass loss ratios from triplicate tests for (a) discs; (b) rods, various dimensions; and (c) tubes, $D_o = 12$ mm. Data in (a) and (b) for the three diameters are plotted at offset temperatures for clarity. Range bars correspond to maximum and minimum values. Horizontal dashed lines indicate $\Delta m_{end} = m_{alc}$.

Figure 3 Schematic of shrinking core model for an infinitely long cylinder of radius R .

Figure 4 Effect of sample geometry on ideal one-dimensional drying behaviour: effect of aspect ratio on area ratio for (a) discs and (b) rods. Solid lines show analytical relationships, data points represent the geometries employed in experiments. Range bars in (a) indicate the effect of variation in disc thickness (*e.g.* average thickness $2H = 3$ mm, minimum is 2.5 mm, maximum is 4 mm). Range bars for cylindrical samples are too small to be shown clearly in (b).

Figure 5 Comparison of results from numerical simulations of Fickian diffusion in finite rods (open symbols) with experimental data (solid symbols) and the analytical 1-D result (Equation (16), solid line). $D_o = 20.5$ mm at 60°C in all cases. Numerical simulations: L/D_o of 1, 2, 5 and 10 using D_{eff} values of 2.0, 1.6, 1.1 and $1.0 (\times 10^{-10} \text{ m}^2 \text{ s}^{-1})$, respectively. The Fo_M values for the experimental data sets ($L/D_o = 10$) were calculated using $D_{eff} = 1.08 \times 10^{-10} \text{ m}^2 \text{ s}^{-1}$.

Figure 6 Application of the shrinking core model [Equation (8)] to the drying of rods with $D_o = 12.0$ mm and $L/D_o = 10$ at (a) 40°C and (b) 100°C . Note different time scales. k_{sc} values for the three rod geometries ($D_o = 12.0$ and 20.5 mm, both with $L/D_o = 10$; and $D = 30.2$ mm, $L/D = 2$) at (c) 40°C and (d) 100°C . Range bars indicate minimum and maximum values obtained.

Figure 7 Examples of fitting analytical Fickian diffusion models (Eqs 14 and 16) to data sets from (a) discs and (b) rods at (i) 40°C and (ii) 100°C .

Figure 8 Effect of temperature on D_{eff} extracted from data for (a) discs with different diameters and (b) rods with different diameters and $L/D_o = 2$. Range bars indicate maximum and minimum values obtained.

Figure 9 Comparison of D_{eff} values obtained by fitting data to 1-D models geometries in the temperature range 40 - 100°C . The x co-ordinate is the value obtained from discs with $H = 1.5$ mm at a given temperature: the y co-ordinate reports the value obtained from rods of different diameters and lengths (see legend). The increase in D_{eff} for each data set corresponds to the increase in temperature. Dashed line indicates locus of equality.

Figure 10 Tube drying at (a) 50°C and (b) 90°C for $D_o = 12.0$ mm and $L/D_o = 10$. Note different time scales. Solid lines show fits of the Crank model for cylindrical geometries [Equation (16)] and dashed lines for tubular geometries [Equation (18)].

Figure S1 Effect of aspect ratio: averaged mass loss data from triplicate tests for disc diameters $D_o = 12.0, 20.5$ and 30.2 mm, $H = 1.5$ mm, at drying temperatures of (a) 40°C and (b) 100°C. Note different time scales. Horizontal dashed lines indicate $\Delta m = m_{alc}$.

Figure S2 Effect of aspect ratio for rods: averaged mass loss data from triplicate tests on cylindrical rods with $D_o = 12.0$ mm at 100°C. Horizontal dashed line indicates $\Delta m = m_{alc}$. Range bars (similar to symbol size) indicate examples of minimum and maximum values obtained.

Figure S3 Drying of a 30.2 mm diameter disc at 40°C: data plotted in the form expected for the shrinking core model, Equation (9).

Figure S4 Pseudo-Arrhenius plot showing effect of temperature on k_{sc} values obtained from rods with $D_o = 12.0$ mm, $L/D_o = 10$; $D_o = 20.5$ mm, $L/D_o = 10$, and $D_o = 30.2$ mm, $L/D_o = 2$. Range bars indicate minimum and maximum values.

Table 1

Table 1 Sample geometries, dimensions and test temperatures for the isothermal drying tests. Ticks indicate the tests performed. For meaning of symbols, see nomenclature.

Geometry	Dimensions (mm)			Temperature (°C)						
				40	50	60	70	80	90	100
Discs	D_o	H								
	12.0	~ 1.5		✓	✓	✓	✓	✓	✓	✓
	20.5	~ 1.5		✓	✓	✓	✓	✓	✓	✓
	30.2	~ 1.5		✓	✓	✓	✓	✓	✓	✓
Rods	D_o	L								
	12.0	12, 24, 60, 120, 240		✓		✓		✓		✓
	20.5	20, 40, 100, 200		✓		✓		✓		✓
	30.2	30, 60		✓		✓		✓		✓
Tubes	D_i	D_o	L							
	0	12	120		✓		✓		✓	
	2	12	120		✓		✓		✓	
	4	12	120		✓		✓		✓	
	8	12	120		✓		✓		✓	

Table 2 Averaged D_{eff} values (in $10^{-10} \text{ m}^2 \text{ s}^{-1}$) from triplicate tests for drying of disc samples.

Disc diameter D_0 (mm)	Temperature ($^{\circ}\text{C}$)						
	40	50	60	70	80	90	100
12.0	1.01	1.46	1.68	2.43	3.30	3.57	6.08
20.5	0.75	0.84	1.24	1.71	2.19	3.16	5.70
30.2	0.54	0.79	1.07	1.28	2.04	2.70	3.72

Table 3

Table 3 Averaged D_{eff} values (in $10^{-10} \text{ m}^2 \text{ s}^{-1}$) from triplicate tests for rod samples. (-) indicates that no test was performed.

(a) $L/D_0 = 1$	D_0 (mm)	40 °C	60°C	80°C	100°C
	12.0	0.96	1.86	2.48	3.63
	20.5	1.31	1.88	3.80	5.91
	30.2	2.16	2.41	5.36	9.26
<hr/>					
(b) $L/D_0 = 2$	D_0 (mm)	40 °C	60°C	80°C	100°C
	12.0	0.56	0.84	1.93	2.50
	20.5	0.99	1.44	2.90	4.46
	30.2	1.83	2.13	5.07	7.61
<hr/>					
(c) $L/D_0 = 5$	D_0 (mm)	40 °C	60°C	80°C	100°C
	12.0	0.44	0.87	1.66	1.91
	20.5	0.86	1.10	2.64	3.96
	30.2	(-)	(-)	(-)	(-)
<hr/>					
(d) $L/D_0 = 10$	D_0 (mm)	40 °C	60°C	80°C	100°C
	12.0	0.32	0.59	1.15	1.69
	20.5	0.83	1.08	2.36	3.41
	30.2	(-)	(-)	(-)	(-)
<hr/>					
(e) $L/D_0 = 20$	D_0 (mm)	40 °C	60°C	80°C	100°C
	12.0	0.40	0.42	0.83	(-)
	20.5	(-)	(-)	(-)	(-)
	30.2	(-)	(-)	(-)	(-)

Table 4 Averaged D_{eff} values (in $10^{-10} \text{ m}^2 \text{ s}^{-1}$) from triplicate tests for extruded tube and rod samples with $D_o = 12.0 \text{ mm}$ and $L/D_o = 10$.

D_i (mm)	50 °C	70 °C	90 °C
0 (solid rod)	0.30	0.59	0.93
2	0.21	0.45	0.90
4	0.21	0.48	1.06
8	0.21	0.43	0.74

Figure 1

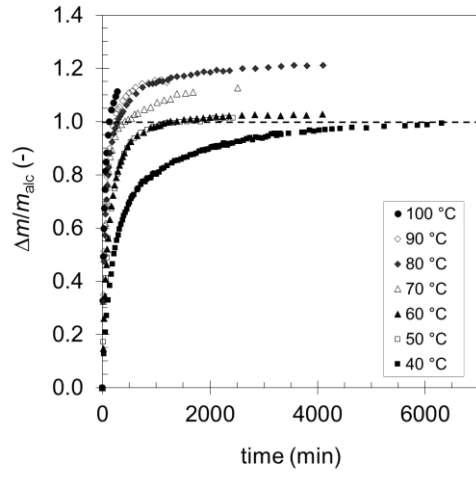
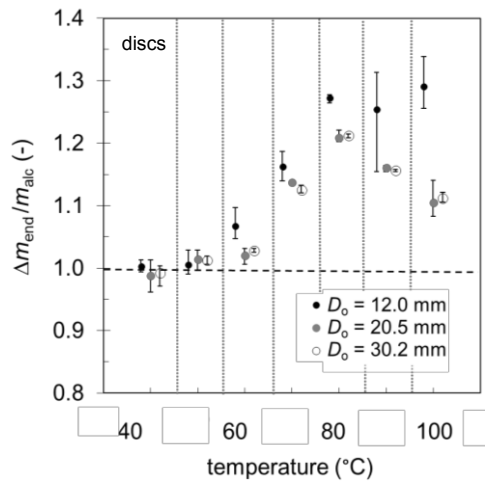
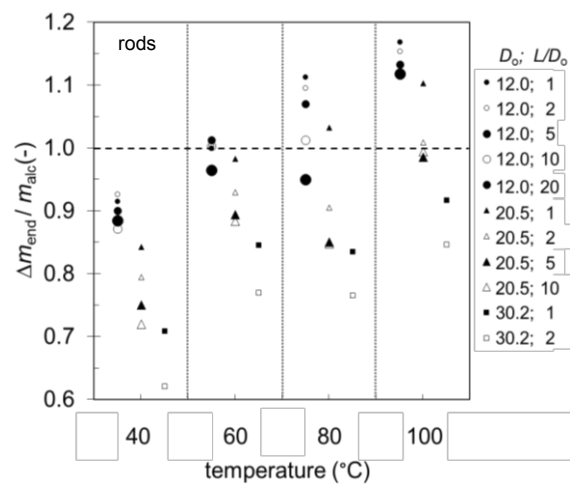


Figure 2

(a)



(b)



(c)

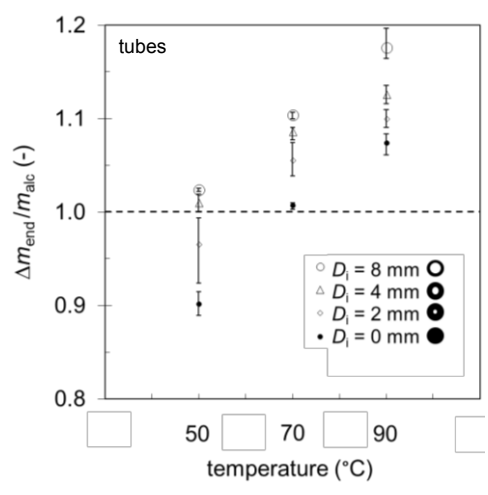


Figure 3

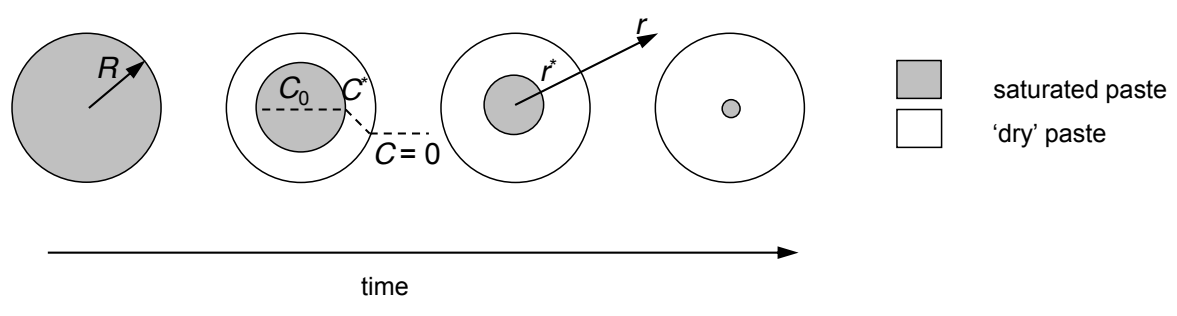


Figure 4

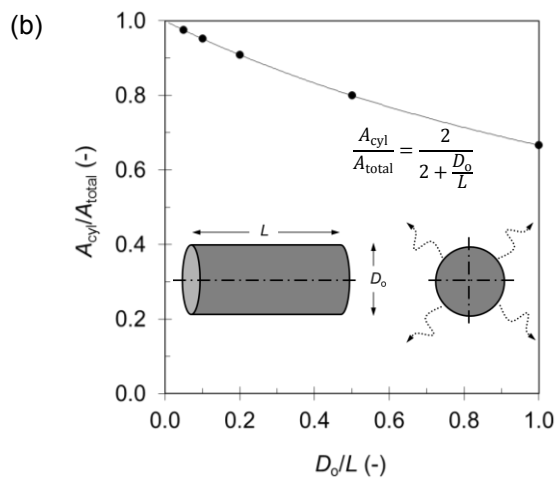
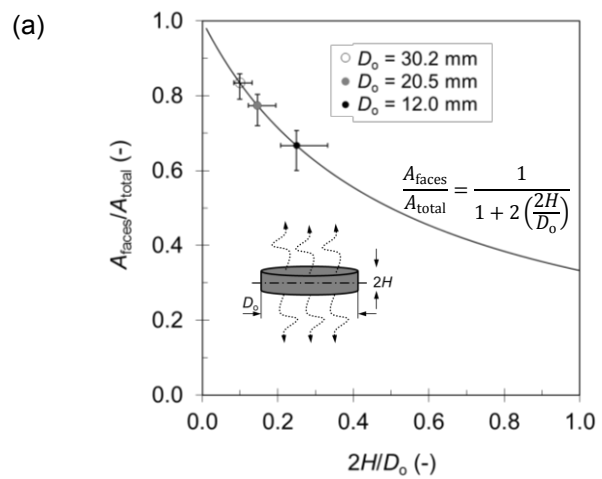


Figure 5

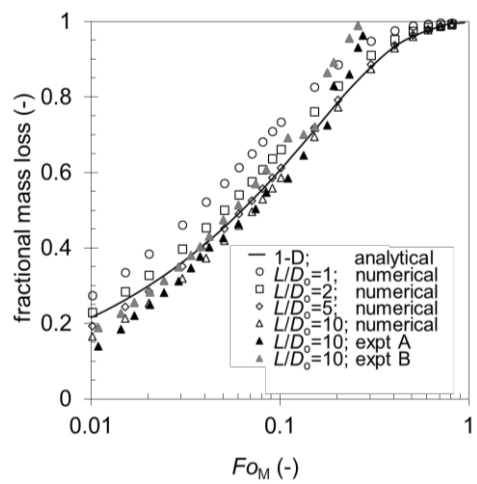


Figure 6

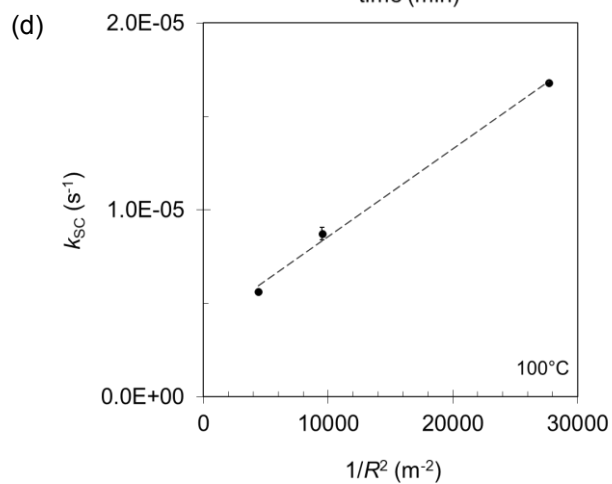
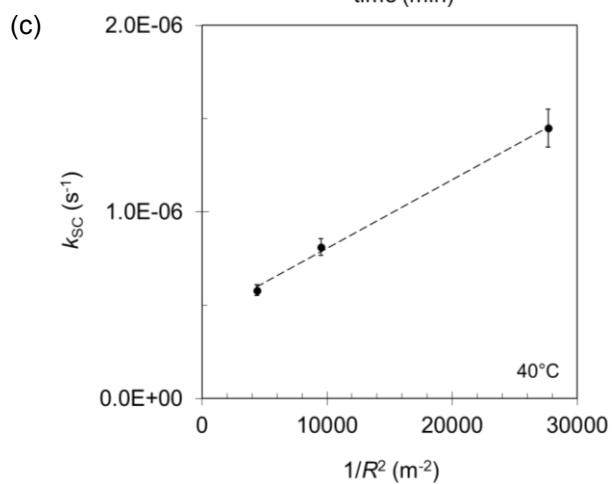
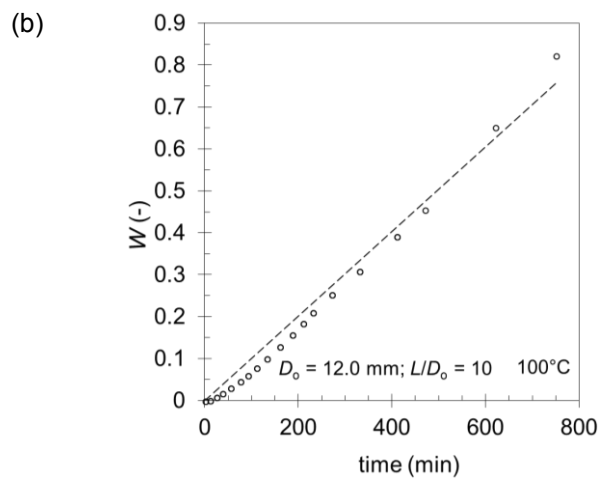
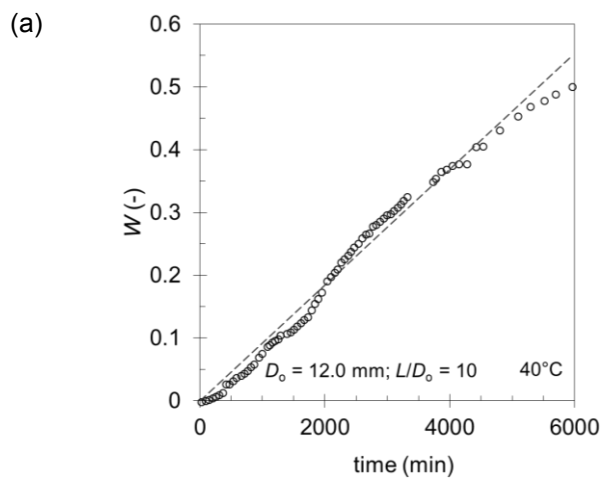
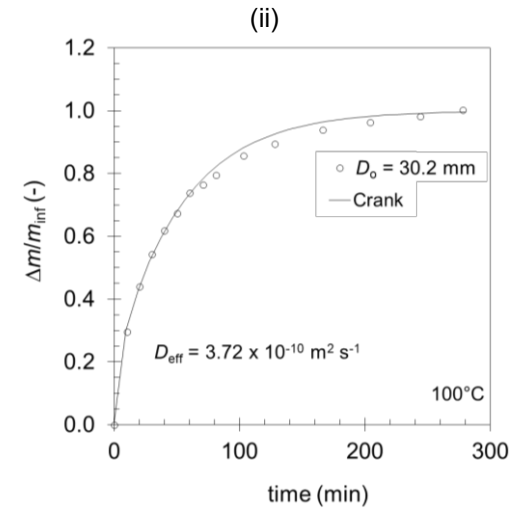
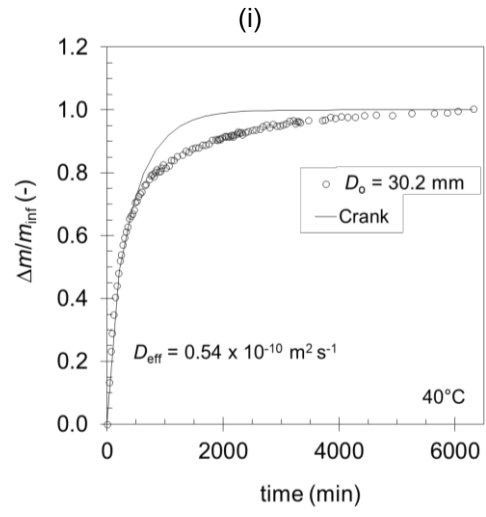


Figure 7

(a)



(b)

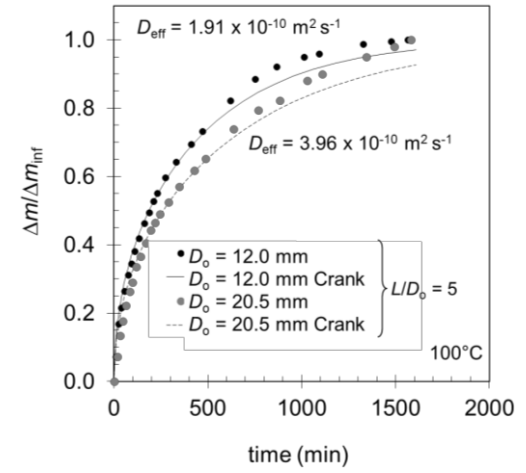
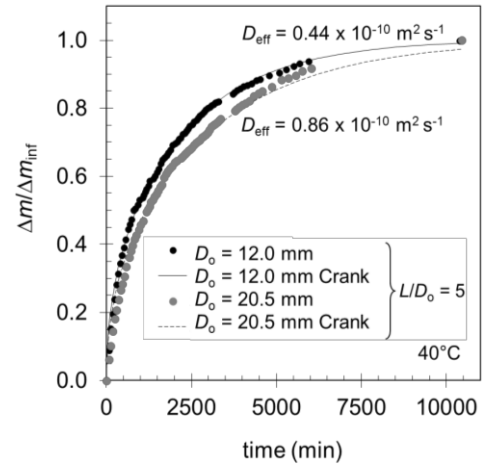


Figure 8

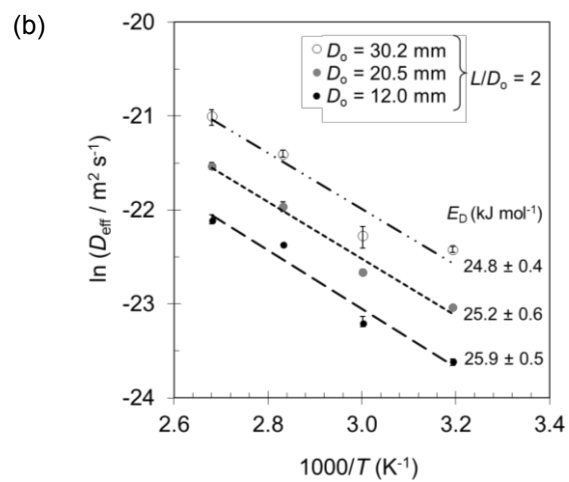
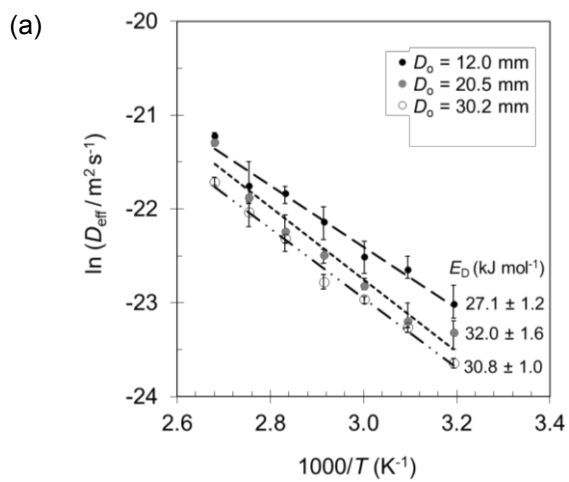


Figure 9

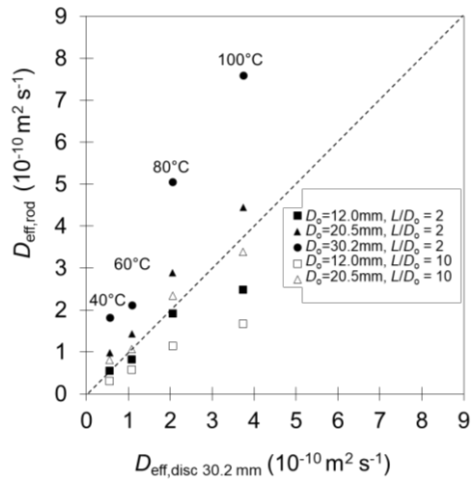
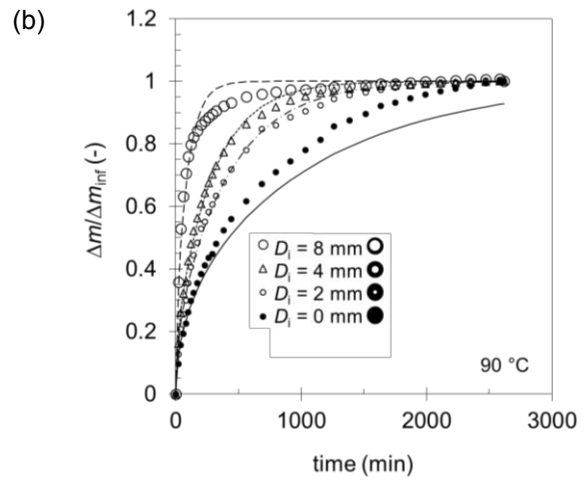
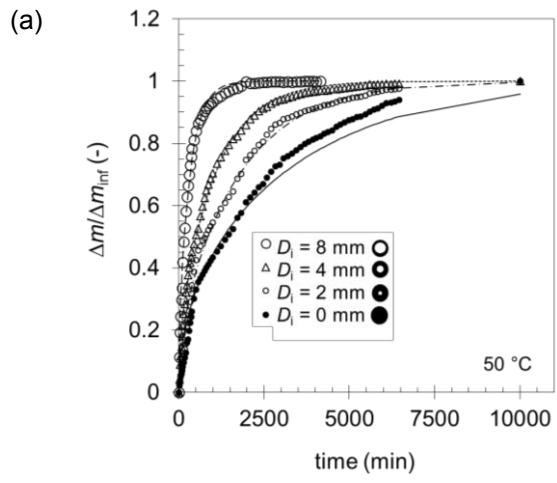
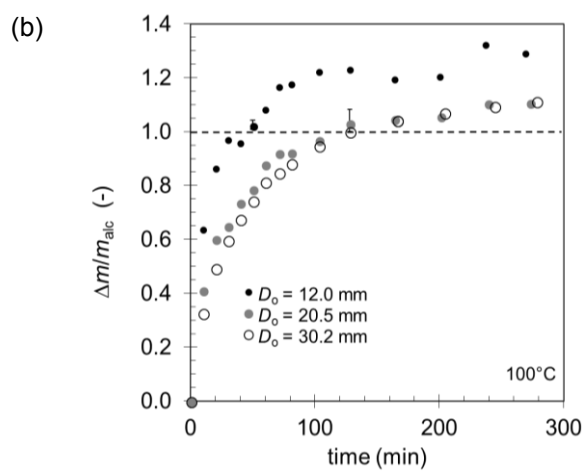
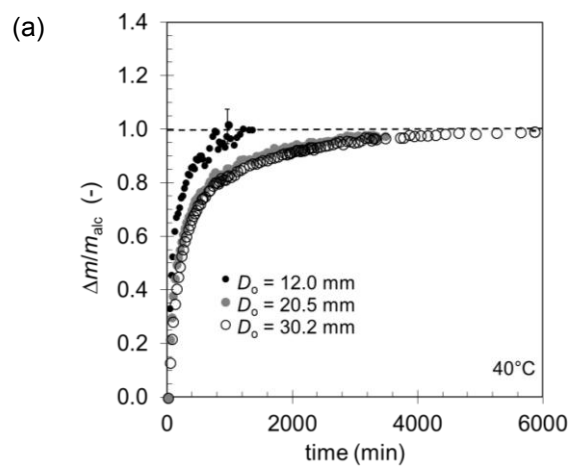
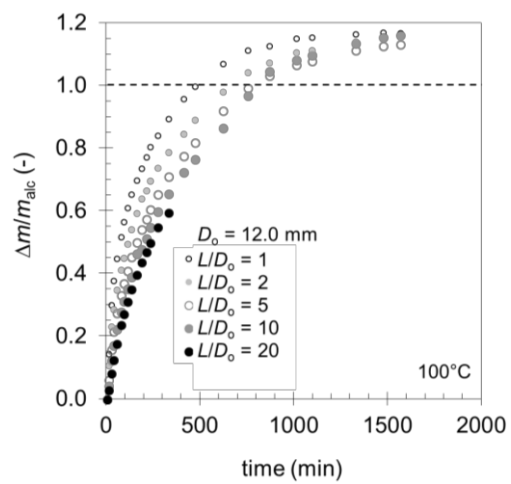


Figure 10





Supplementary Figure S2



Supplementary Figure S3

